Abstract of Paper Proposed for Presentation at the
43rd AIAA Aerospace Sciences Meeting and Exhibit
Reno, NV
10–13 January, 2005

Characterization of Space Shuttle Ascent Debris using CFD Methods

Scott M. Murman*
ELORET
MS T27B
Moffett Field, CA 94035
smurman@nas.nasa.gov

Michael J. Aftosmis† and Stuart E. Rogers‡
NASA Ames Research Center
MS T27B
Moffett Field, CA 94035

1 Introduction

After video analysis of space shuttle flight STS-107's ascent showed that an object shed from the bipod-ramp region impacted the left wing, a transport analysis was initiated to determine a credible flight path and impact velocity for the piece of debris. This debris transport analysis was performed both during orbit, and after the subsequent re-entry accident. The analysis provided an accurate prediction of the velocity a large piece of the foam bipod ramp would have as it impacted the wing leading edge (cf. [1], pg. 61). This prediction was corroborated by video analysis and fully-coupled CFD/6-DOF simulations[2]. While the prediction of impact velocity was accurate enough to predict critical damage in this case, one of the recommendations of the Columbia Accident Investigation Board

*Senior Research Scientist, Member AIAA
†Aerospace Engineer, Senior Member AIAA
‡Aerospace Engineer, Associate Fellow AIAA

(CAIB) for return-to-flight (RTF) was to analyze the complete debris environment experienced by the shuttle stack on ascent. This includes categorizing all possible debris sources, their probable geometric and aerodynamic characteristics, and their potential for damage. This paper is chiefly concerned with predicting the aerodynamic characteristics of a variety of potential debris sources (insulating foam and cork, nose-cone ablator, ice, ...) for the shuttle ascent configuration using CFD methods. These aerodynamic characteristics are used in the debris transport analysis to predict flight path, impact velocity and angle, and provide statistical variation to perform risk analyses where appropriate. The debris aerodynamic characteristics are difficult to determine using traditional methods, such as static or dynamic test data, due to the scaling requirements of simulating a typical debris event. The use of CFD methods has been a critical element for building confidence in the accuracy of the debris transport code by bridging the gap between existing aerodynamic data and the dynamics of full-scale, in-flight events.

In order to provide an efficient engineering tool, the debris transport code simplifies several aspects of the problem. The first approximation is that the debris has no effect on the flowfield: the transport code queries the local flow conditions from a high-resolution, static, viscous flow simulation of the shuttle flowfield provided by the OVERFLOW solver[3] at the appropriate flight conditions for the debris event. A ballistic model is applied in the direction of the local flow velocity to determine the deceleration and "zero-lift" trajectory. The version of the debris transport code used in the STS-107 investigation applied an initial velocity to the debris in order to simulate the dispersion due to aerodynamic lift. The code does not directly account for any potential rotation of the body. With these approximations the debris transport code can analyze a single debris trajectory through the shuttle flowfield in seconds of CPU time, while simulating the dynamic fully-coupled 6-DOF problem requires hundreds of CPU-hours. Without sacrificing this efficiency, it is desired to improve the accuracy of the debris transport code. These improvements include a realistic modeling of the dispersions about the zero-lift trajectory due to aerodynamic lift, and drag models tailored to the different debris sources. Both of these enhancements to the transport code require a detailed knowledge of the aerodynamics of free-flying pieces of debris.

The characterization of the flight dynamics for shuttle ascent debris involves developing models and/or databases of aerodynamic parameters for each type of debris which are then integrated with the requirements of the debris transport code. This then involves developing drag models for use in the ballistic, zero-lift trajectory computation, and crossrange models to superimpose the effect of lift on a trajectory. The current work describes the use of a Cartesian mesh, moving-boundary solver[4] to efficiently provide the data for developing the drag and crossrange models. The Cartesian package can automatically handle arbitrary geometric shapes, and perform steady-state, prescribed-motion, or fully-coupled 6-DOF simulations using an efficient parallel, multi-level algorithm. This provides the analyst with a push-button tool for simulating static wind tunnel, rotary-balance, or ballistic range tests computationally. This ability is used to complement and extend the traditional physical test facilities providing a cost-effective approach for aerodynamic modeling of these complex dynamic events.

The analysis of the shuttle ascent debris environment is an iterative process (cf. Fig. 1). The debris sources and their aerodynamic characteristics are fed into the debris transport code, which calculates trajectory information to provide an assessment of the potential damage or risk from a particular debris source for a particular structural component (i.e. the orbiter wing). This damage assessment is provided to the separate structural components of the shuttle, which are then able to decide whether

they can safely withstand the damage. This structural analysis in turn is fed back into the process, as debris sources which cannot be safely tolerated are eliminated through design modifications.

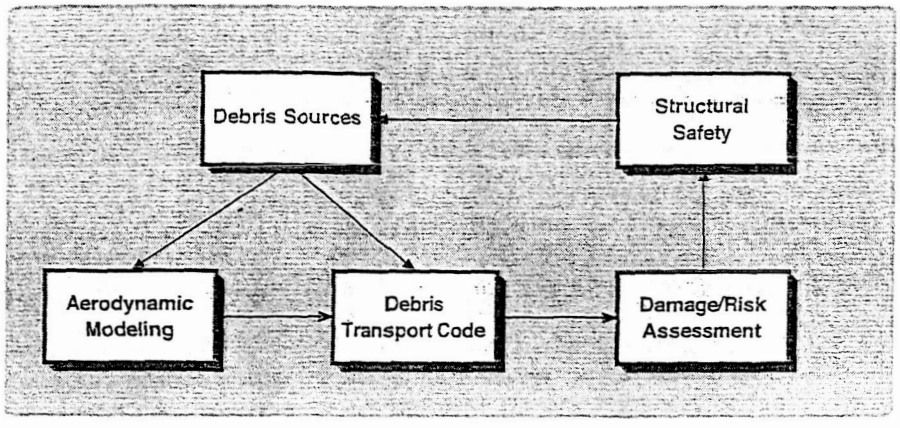

Figure 1: Debris analysis feedback loop. Damage from potential debris sources is assessed, and those which are not tolerable are eliminated. This cycle then continues until a safe tolerance is achieved.

The current abstract provides a general overview of the types of debris analyzed to-date, the effort underway to validate the CFD solver for these types of complex dynamic trajectories, and the current level of aerodynamic modeling for external tank (ET) foam. The proposed full paper will include a detailed review of the ascent debris environment, and include refined aerodynamic models for the various debris types, as well as experimental data for direct comparison.

2 Debris Sources

As a first step, all of the potential debris sources for the space shuttle stack on ascent must be categorized. The primary debris sources can be categorized as spray-on foam insulation for the ET, resinous cork insulation for the SRB*, ablator material from the SRB nose cones, and frost ice which forms due to condensation on the ET. The dynamic behavior of any debris piece, and by extension the aerodynamic modeling of any debris piece, is dependent upon the shape of the debris. Figure 2a has photographs of divots which were "popped-off" from the 1"-thick foam which covers the ogive section of the ET (so-called acreage foam) during experimental tests. These pieces are roughly conical-shaped (a truncated cone, or frustum), and can vary in diameter, thickness, and conical bevel angle. Figure 2b contains similar photographs of two foam divots which were ejected from the 3"-thick ET inter-tank flange foam which separates the region between the liquid hydrogen and liquid oxygen tanks inside the ET. These shapes are larger, and more irregular than the acreage divots, due to the greater depth of foam in these locations.

The size and shape of the SRB cork material has been estimated from "closeout" photos which are taken as the SRBs separate from the shuttle stack. These pieces are modeled as thin parallelepipeds. Ice and ablator still remain for analysis, and will be included in the final paper. The material properties, and estimates of the relevant dimensions of the debris types are supplied in Table 1.

*This is a man-made material, similar in construction to particle-board, not natural cork.

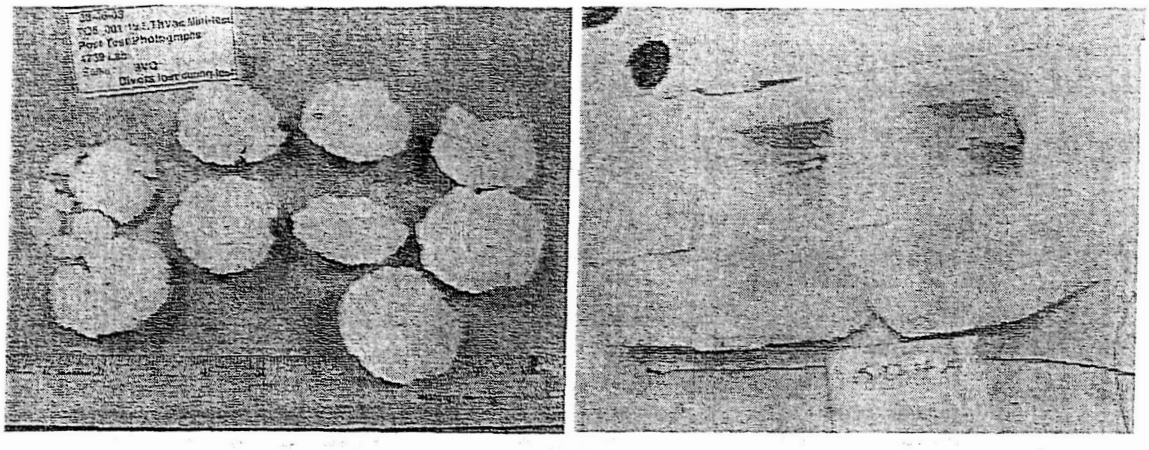

(a) Divots from ET ogive acreage foam

(b) Divots from ET flange foam

Figure 2: Divots "popped-off" from ET foam slabs during experimental testing.

Material	Density (lbm/ft^3)	Max. Dimension (in.)	Approx. Thickness (in.)
ET foam	2.4	6.0	1.0
SRB cork	31.3	12.0	1.0
ice	57.25	TBD	TBD
SRB ablator	TBD	TBD	TBD

Table 1: Debris material properties and dimensions.

3 Verification and Validation

Characterizing the aerodynamics of dynamic debris shedding events from the shuttle stack on ascent requires the ability to efficiently compute static, prescribed-motion, and coupled 6-DOF simulations. The implicit Cartesian moving-boundary solver described in [4] and [5] fulfills these requirements. The mesh generation is automated, and parameter studies of the various dynamic scenarios experienced by the debris are automatically handled by the Geometry Manipulation Protocol (GMP) interface [6]. The aerodynamic characterization investigates an isolated piece of dynamic debris in a uniform stream, moving under the influence of aerodynamic forces. This results in a time-dependent coupling between the fluid dynamics and the motion of the body. This coupled CFD/6-DOF scenario is efficiently and accurately simulated using the Arbitrary Lagrangian-Eulerian (ALE) rigid-domain motion capability of the solver. This allows the motion of the debris to be handled entirely within the software of the flow solver without requiring complicated and costly inter-mesh communications between timesteps. Complete details on the numerical algorithms are presented in [4] and [5].

3.1 Viscous Comparison

The Cartesian moving-body solver has been validated for a variety of aerodynamic problems, including store separation, dynamic missile configurations, and transonic flutter[4, 7, 8]. The requirements of simulating debris shedding from the shuttle on ascent are unique however, and further validation for these dynamics is required. The Cartesian moving-body solver currently uses an inviscid approximation. The appropriateness of this approximation is examined by comparing static, bluff-body simulations of a conical acreage foam piece (cf. Fig. 3a) obtained with the Cartesian inviscid solver, and the OVERFLOW viscous, overset solver. The rationale for choosing this comparison experiment will be presented in the next section. The predicted drag coefficient for the relevant Mach number range seen during ascent is presented in Fig. 3b. The maximum variation between the two solvers occurs at Mach = 1.0, and is 8%. The viscous increment is essentially zero ($< 0.1\%$) for these calculations. The only faces which can effect the viscous drag are the beveled sides, which are located in the aft separated flow region. These aft faces experience reversed and separated regions, which when time-averaged, provide essentially no viscous stress contribution. While the viscous increment itself is negligible, the differences between the calculations at the lower Mach numbers are due to viscous effects. The viscous flow has stronger shear layers, which form stronger vortices, and also has a much wider energy band (contains energy at a range of frequencies) than the inviscid calculations which tend to have energy only at the shedding frequency. The stronger aft vortices induce an unsteady flow at a slightly higher Mach number in the viscous calculations (Mach = 1.4 vs. Mach = 1.2). Beyond these Mach numbers the flowfield remains steady. At the lower Mach numbers (0.6 and 0.8), these stronger vortices induce a stronger reversed flow. This stronger reversed flow creates a lower pressure on the aft face of the body, and leads to a slightly higher drag. So in general we would expect the inviscid calculations to slightly underpredict the drag, though not to the lack of a viscous increment. These stronger shear layers also appear to cause the discrepancy at Mach = 1.0. The wider separated region makes the body look slightly larger.

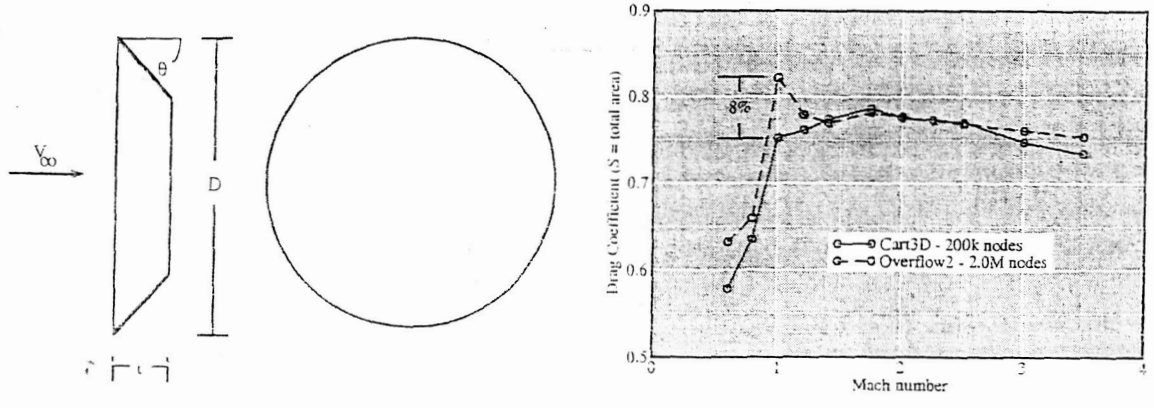

(a) Conical ET acreage foam (D = 6", θ = 58°, 0.013 lbm)

(b) Drag coefficient variation

Figure 3: Drag coefficient variation for a conical acreage divot in a static, bluff-body orientation through the shuttle ascent Mach number range.

Figure 3 demonstrates that an inviscid solver provides an efficient engineering approximation for these supersonic separated, bluff-body flows. The computational cost of computing a single 6-DOF trajectory using the Cartesian solver solver is nearly two orders of magnitude lower than the same trajectory computed with OVERFLOW, due to the stiffness and mesh requirements of the viscous solver. This efficiency allows a range of debris sources and release conditions to be examined computationally, so that broad behavioral trends can be discerned, rather than examining a handful of datapoints.

3.2 Dynamic Cube Validation

The previous section considers static simulations, however a validation of dynamic predictions must be considered as well. Unfortunately there is a dearth of appropriate data for extremely light objects being released at high Mach numbers and high altitude. Hansche and Rinehart[9] fired 1/4" and 3/8" steel cubes from a gun at sea-level and measured the drag as a function of Mach number. This data is especially relevant for comparison as the ballistic drag model used in the debris transport code for the STS-107 investigation is based upon this data, i.e. all debris sources are assumed to be roughly shaped like cubes. Obviously the validity of this assumption for conical shapes like Fig. 3a is questionable. Figure 4 presents the computed drag coefficient variation against the experimental data, using several different simulation methods. The red and blue curves were computed with the cube held fixed with the minimum and maximum frontal area exposed to the wind respectively. These static computations mirror the lower and upper bounds of the experimental scatter. In order to simulate an "average" tumbling dynamic motion, the cube was rotated at a constant rate about all three axes at a fixed Mach number. The average of these dynamic simulations over a complete cycle is termed a "forced-tumble" simulation. The forced tumble results for the cube bisect the experimental data. The final type of simulation included in Fig. 4 is a 6-DOF simulation with the cube being released into a uniform stream and allowed to decelerate and rotate under the influence of the aerodynamic forces. This dashed green curve shows the cube begin to oscillate as the separation buffets the body, eventually leading to a tumbling motion as the cube passes through the transonic regime. The drag prediction from the 6-DOF trajectory again falls within the experimental data. Of note here is that the cube does not tumble immediately. The cube is statically-stable in a supersonic flow, which is a necessary, but not sufficient, condition to ensure dynamic stability. Since the inertia of these small cubes is very low, the rotational inertia of the cube is not sufficient to overcome the static stability (unless the cube is rotated at unrealistically high rates). Simulations in which the cube is initially rotated and then released exhibit the same behavior - an oscillation about the static stability point in supersonic flow, and a tumbling motion in the transonic regime as the dynamic pressure decreases sufficiently so that the restoring aerodynamic moment on the cube is not sufficient to maintain the stable oscillation. This same type of dynamic behavior will be seen in the results for the conical foam divots in the next section.

3.3 Mars Smart Lander

Current work is simulating ballistic range experiments performed at the NASA Ames Hypervelocity Free Flight Aerodynamics Facility (HFFAF) with the Mars Smart Lander (MSL) configuration[10].

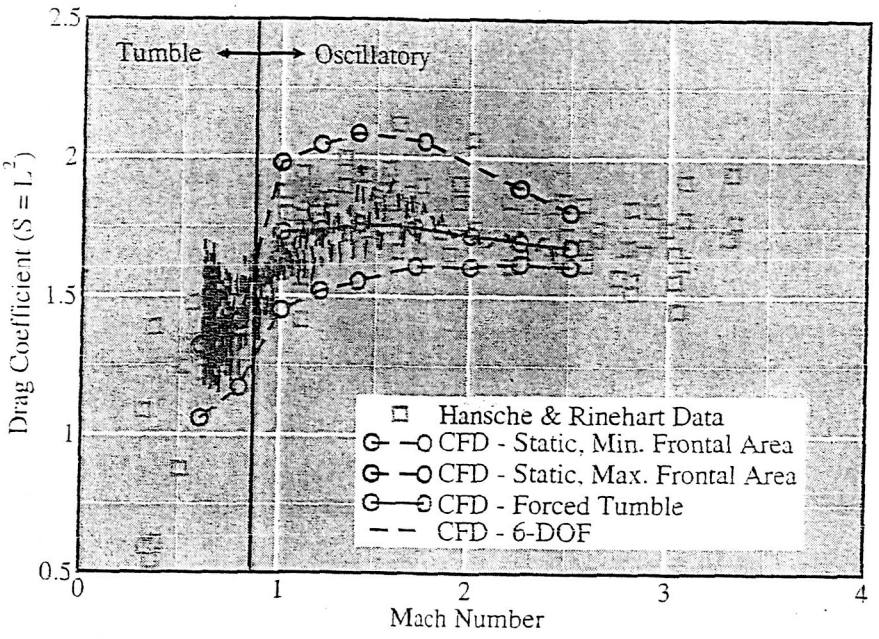

Figure 4: Drag coefficient variation for a cube. Static, forced-tumble, and 6-DOF simulations are compared against ballistic range data from [9].

The MSL configuration is pictured in Fig. 5. While not a true thin conical divot, the MSL configuration is geometrically similar, in that it has a bluff forebody which trims the MSL in a bluff-body orientation in supersonic flight. Computations simulating the supersonic test firings from [10] are intended to validate the ability of the Cartesian solver to reproduce angular rate data, as well as drag predictions, and as an aid for establishing data requirements for dynamic tests of foam articles. Dynamic testing of conical foam shapes is currently in the planning stages. The full paper will include a complete comparison against the MSL data, as well as any relevant ballistic range data for foam insulation.

4 Foam Debris

Figure 2 shows photographs of foam divots which were either forced from foam sheets, or ejected due to voids containing trapped air. As experimental evidence on the typical shapes and sizes of foam continues to accumulate the accuracy with which particular shapes can be digitally mimicked increases. One of the early experiments observed that the foam tended to eject as a truncated frustum, with a bevel angle of roughly 45°. Initial computational efforts to characterize the foam aerodynamics thus concentrated on frustum shapes of various dimensions, having a bevel angle of $\theta = 45°$. The difference between a modeled axisymmetric frustum shape and the experimental evidence of Fig. 2 highlights the difficulty involved in modeling the debris aerodynamics for use in a ballistic code. A debris piece whose shape and size is only generally known is proposed to shed from a particular

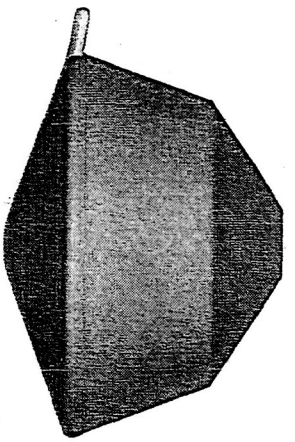

Figure 5: Mars Smart Lander configuration[10]

location. The velocity and angular rotation of this shedding event are unknown, and in fact the debris may linger in the boundary layer until popping into a high-speed stream. Trajectory calculations are inherently sensitive initial-value problems, yet in our modeling we cannot accurately state any of the initial conditions! Predicting any single trajectory is thus an impossibility, and the approach taken here is to predict an average trajectory. With this average trajectory in-hand, variations (for lift, drag, etc.) can then be superimposed.

4.1 Drag

A series of simulations of frustum shapes of varying dimensions was undertaken using the static, forced-tumble, and unconstrained 6-DOF techniques demonstrated in Sec. 3.2 for the dynamic cube data. An example for a $D = 9"$, $t = 3"$ piece (cf. Fig. 3) with mass of 0.22 lbm is shown in Fig. 6. Here the static broadside data and the forced-tumble data are provided along with three sample unconstrained 6-DOF trajectories. In the sample 6-DOF trajectories the frustum is either released from a static, edge-on orientation or initially rotating about all three axes at 20 Hz before release. The static release trajectory closely follows the static bluff body drag variation, and the frustum only oscillates slightly before finally tumbling at lower Mach number as the dynamic pressure (and aerodynamic restoring moment) decreases. The initially rotating trajectories display a greater variation, however again the pieces oscillate without tumbling in the supersonic regime. The largest variation occurs when the initially rotating piece is released in an edge-on configuration, so that the oscillation is nearly $\pm 90°$ relatively to the static stability point, and hence the drag is closer to the forced-tumble than static data. This behavior is similar to the cube dynamics discussed in Sec. 3.2, and is caused by the low inertia of these foam pieces coupled with a relatively strong static stability point in the bluff-body configuration. In order to overcome the static stability with such low inertia, the rotational rate must be implausibly high.

While the dynamic behavior exhibited by the foam frustum pieces is complex, an important observation from Fig. 6 is that the ensemble average of the 6-DOF trajectories is bounded by the static and forced-tumble data. This bounding is observed in all of the foam pieces simulated to-date.

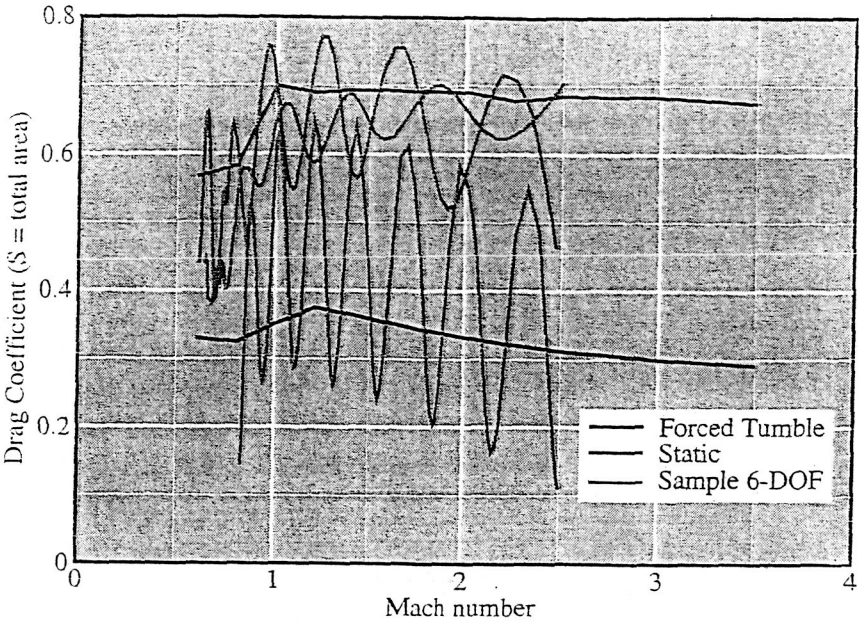

Figure 6: Drag variation for static bluff-body, forced-tumble, and sample 6-DOF trajectories for a 0.22 lbm frustum.

Recall that the goal for this work is to model an average trajectory. While we can bound the behavior of a single frustum foam piece, we still require a method of characterizing the behavior of a range of foam pieces. The proposed solution is to use an ensemble average of the bounding curves for each frustum piece tested. These tested pieces span the range of $D = 1.8" - 12"$, $t = 0.5 - 3"$, and mass = $0.002 - 0.22$ lbm. Further, we need a method of scaling the drag coefficient from these disparately-sized pieces that can collapse a range of data to a single curve. The use of the frustum total area provides this desired scaling. Since the frustum pieces are beveled, the sides are always contributing to drag, as opposed to a piece such as a cylinder, where an axial elongation can change the total area without appreciably changing the drag. This convenience of geometry allows the data from the range of frustum pieces examined to collapse to a within $\pm$ 10% in drag variation relative to the average. The static drag variation with Mach number for all of the simulated frustum pieces is presented in Fig. 7, along with the ensemble average and a 10% variation.

The ensemble average for the range of foam pieces of the static, bluff-body drag is proposed to characterize the drag of ET acreage foam. The use of the static bounding curve is considered conservative, but realistic, approximation. Since we are averaging over a range of pieces this bounding curve is not a hard bound - it is possible for 6-DOF trajectories of some pieces to exhibit a drag higher than the modeled drag. This is demonstrated by examining the variation of kinetic energy (which is a good corollary for damage potential) with distance traveled. Figure 8 presents the kinetic energy against the distance traveled for a 0.22 lbm frustum released at $M_\infty = 2.5$ in a uniform stream calculated with a ballistic code using three different drag models: the tumbling cube data from Sec. 3.2 which was used for the STS-107 investigation, an ensemble average of the tumbling frustum drag, and an ensemble average of the static frustum drag. The observation is that the average trajectory

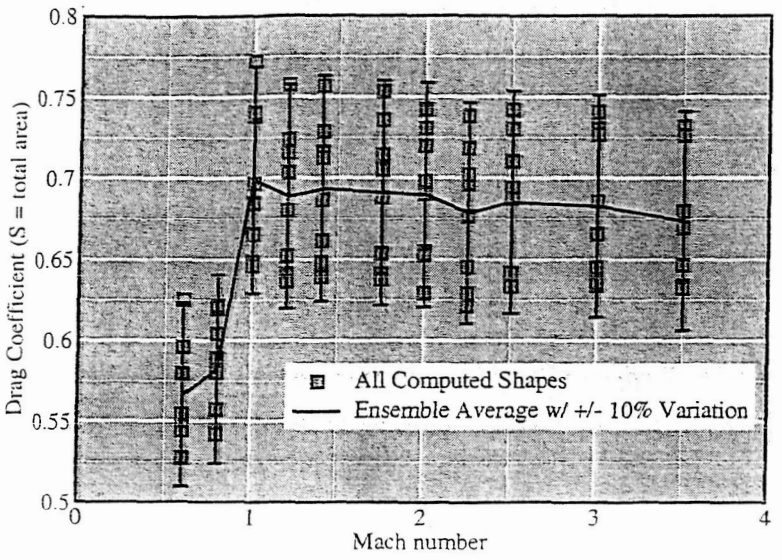

Figure 7: Ensemble average of static bluff-body drag over all frustum pieces examined.

for an ET acreage divot will lie between the static and tumbling frustum curves, though individual trajectories can exceed these bounds. Note that the tumbling cube model severely underpredicts the kinetic energy relative to the other models. This is not caused by the cube having a larger drag, rather that the frustum has a much larger acceleration than the cube. For a given mass, the frustum roughly maximizes the drag (and hence the acceleration), while the cube roughly minimizes the drag for a fixed mass. Thus, while the tumbling cube data is accurate, it is only appropriate for use in modeling cubes. Figure 9 presents samples of the kinetic energy variation with distance for three shapes: a 0.22 lbm $\theta = 45°$ frustum, a 0.014 lbm $\theta = 58°$ frustum, and a digitized ET flange divot from Fig. 2b. Each plot contains the average trajectory for each piece, along with the approximate minimum and maximum drag trajectories. Individual trajectories exceed the ensemble average bounding curves, however the average of all trajectories lies within the bounds.

4.2 Crossrange

The static frustum drag model can be used in the ballistic model, however some method of accounting for the lift generated by each piece must be devised. It is assumed that the lift can act in any direction, so that a crossrange behavior must be superimposed on zero-lift trajectory. Simply using an approximation for L/D for the average piece is not appropriate. The amount of lift a piece can sustain is a function of its inertia: the larger the inertia the longer the debris can sustain a lifting orientation. Similarly, shape and initial conditions play a major role in the lifting behavior. Figure 10 graphically demonstrates one potential approach. A crossrange envelope is developed from

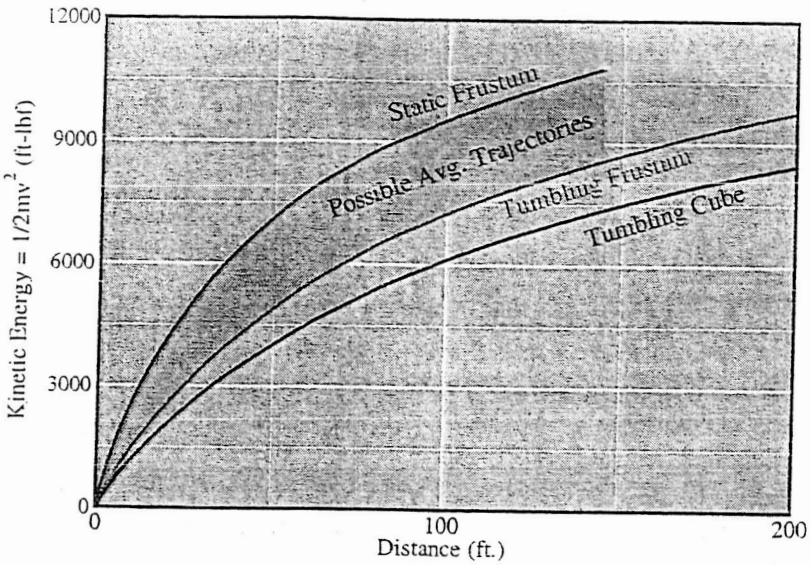

Figure 8: Kinetic energy for a 0.22 lbm frustum released at $M_\infty = 2.5$ in a uniform stream calculated with a ballistic code using three different drag models (see text).

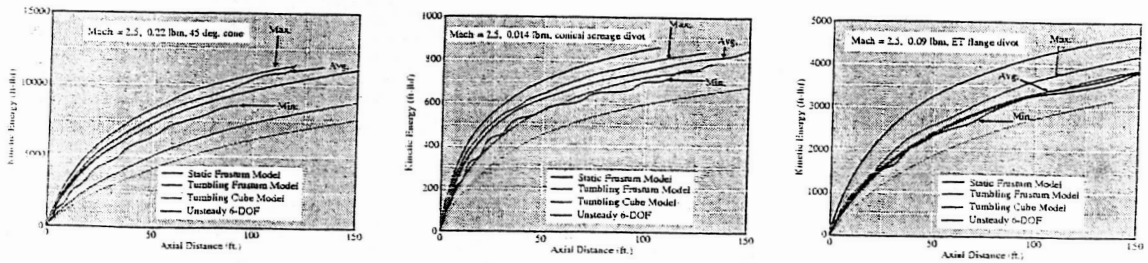

Figure 9: Kinetic energy variation for sample trajectories from a $M_\infty == 2.5$ release, including avgerage, minimum, and maximum.

a Monte-Carlo sampling of debris trajectories. This envelope is a parameterized by distance traveled, Mach number, etc., which can be queried in a simple table lookup from the debris transport code for each trajectory. Further, instead of an envelope, a complete statistical distribution of crossrange behavior can be provided so that a probability function can be queried for each trajectory. Figure 11 presents crossrange behavior from the 6-DOF calculations of two foam debris pieces at release Mach numbers of $M_\infty = 1.4$ and 2.5. The envelope of the crossrange behavior indicates a potential for large excursions, however the majority of the trajectories are contained within a small tube. This information can be directly used in a risk assessment. A similar strategy can be used to determined the flight path angle for each trajectory.

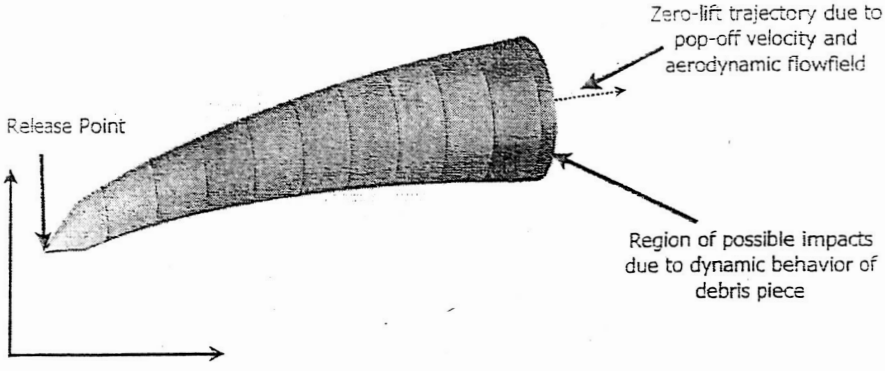

Figure 10: Model of crossflow variation superimposed on a zero-lift trajectory. The envelope of crossrange behavior is colored by flight-path angle.

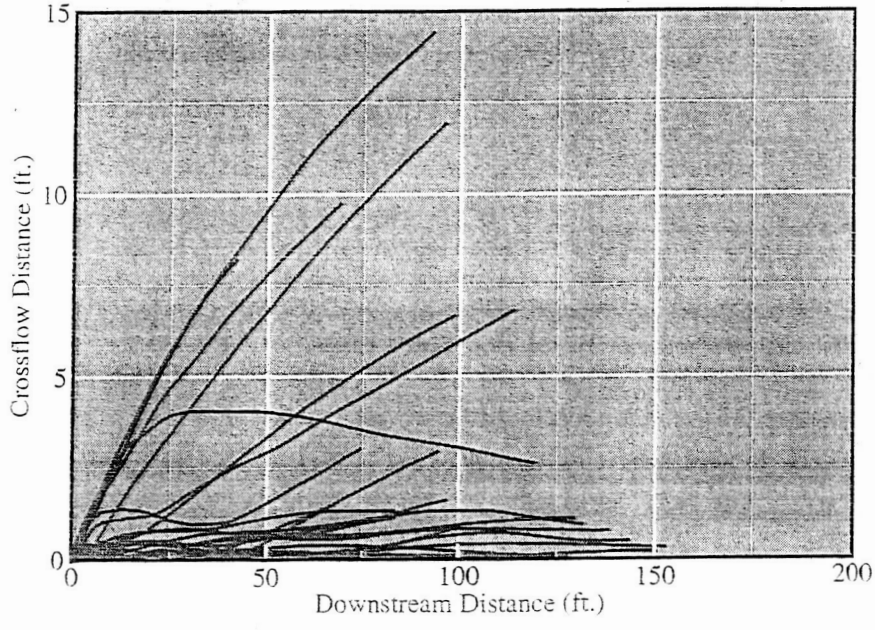

Figure 11: Crossrange behavior for a 0.09 ET flange divot and 0.014 conical acreage foam divot at release Mach numbers of $M_\infty = 1.4$ and 2.5.

The crossrange behavior in Fig. 11 is limited by curves which show a nearly constant lift, however the pieces are typically oscillating and tumbling. This apparently diverse behavior is caused by the piece holding a highly-lifting orientation early in the trajectory. This orientation provides a large crossrange inertia. Since the debris pieces decelerate extremely rapidly, the dynamic pressure drops very quickly, and hence when the piece is in an opposite orientation the restoring force is much smaller. Hence the pieces appear to be constantly lifting, however they are in fact simply responding to an initial "kick" due to orientation that cannot be compensated for later in the trajectory.

5 Future Work

This abstract outlines the debris transport analysis underway within the space shuttle RTF initiative. The aerodynamic characterization of potential debris sources is a key element to this program, and CFD methods have provided necessary data in a cost-effective and timely manner. Details of the aerodynamic modeling for ET acreage foam have been presented in terms of drag and crossrange behavior. Similar models are under development for SRB cork insulation. The final paper will include details of the aerodynamic characterization of all shuttle ascent debris sources analyzed with CFD methods. Further, the use of CFD in developing ballistic range experimental tests, and comparisons with the data derived from these tests, will be included in the final paper.

References

[1] Columbia Accident Investigation Board Report, Vol. 1, Aug. 2003.

[2] Gomez, R.J., Vicker, D., Rogers, S.E., Aftosmis, M.J., Meakin, R.M., Chan, W.M., and Murman, S.M., "STS-107 Investigation Ascent CFD Support," AIAA Paper 2004-2226, July 2004.

[3] Jespersen, D.C., Pulliam, T.H., and Buning, P.G., "Recent Enhancements to OVERFLOW," AIAA Paper 97-0644, Jan. 1997.

[4] Murman, S.M., Aftosmis, M.J., and Berger, M.J., "Implicit Approaches for Moving Boundaries in a 3-D Cartesian Method," AIAA Paper 2003-1119, Jan. 2003.

[5] Murman, S.M., Aftosmis, M.J., and Berger, M.J., "Simulations of 6-DOF Motion with a Cartesian Method," AIAA Paper 2003-1246, Jan. 2003.

[6] Murman, S.M., Chan, W.M., Aftosmis, M.J., and Meakin, R.L., "An Interface for Specifying Rigid-Body Motion for CFD Applications," AIAA Paper 2003-1237, Jan. 2003.

[7] Murman, S.M., Aftosmis, M.J., and Berger, M.J., "Numerical Simulation of Rolling-Airframes Using a Multi-Level Cartesian Method," AIAA Paper 2002-2798, June 2002.

[8] Murman, S.M. and Aftosmis, M.J., "Cartesian-Grid Simulations of a Canard-Controlled Missile with a Spinning Tail," AIAA Paper 2003-3670, Aug. 2003.

[9] Hansche, G.E. and Rinehart, J.S., "Air Drag on Cubes at Mach Numbers 0.5 to 3.5," *Journal of the Aeronautical Sciences*, 19:83–84, 1952. Also *Fluid-Dynamic Drag*, Hoerner, pg. 16–14.

[10] Brown, J., Yates, L., Bogdanoff, D., Chapman, G., Loomis, M., and Tam, T., "Free Flight Testing in Support of the Mars Smart Lander Aerodynamics Database," AIAA Paper 2002-4410, Aug. 2002.